

# Molybdenum Disulfide Nanoribbons with Enhanced Edge Nonlinear Response and Photoresponsivity

Ganesh Ghimire, Rajesh Kumar Ulaganathan, Agnès Tempez, Oleksii Ilchenko, Raymond R. Unocic, Julian Heske, Denys I. Miakota, Cheng Xiang, Marc Chaigneau, Tim Booth, Peter Bøggild, Kristian S. Thygesen, David B. Geohegan, and Stela Canulescu\*

MoS<sub>2</sub> nanoribbons have attracted increased interest due to their properties, which can be tailored by tuning their dimensions. Herein, the growth of MoS<sub>2</sub> nanoribbons and triangular crystals formed by the reaction between films of MoO<sub>x</sub> (2 < x < 3) grown by pulsed laser deposition and NaF in a sulfur-rich environment is demonstrated. The nanoribbons can reach up to 10 μm in length, and feature single-layer edges, forming a monolayer–multilayer junction enabled by the lateral modulation in thickness. The single-layer edges show a pronounced second harmonic generation due to the symmetry breaking, in contrast to the centrosymmetric multilayer structure, which is unsusceptible to the second-order nonlinear process. A splitting of the Raman spectra is observed in MoS<sub>2</sub> nanoribbons arising from distinct contributions from the single–layer edges and multilayer core. Nanoscale imaging reveals a blue-shifted exciton emission of the monolayer edge compared to the isolated MoS<sub>2</sub> monolayers due to built-in local strain and disorder. We further report on an ultrasensitive photodetector made of a single MoS<sub>2</sub> nanoribbon with a responsivity of 8.72 × 10<sup>2</sup> A W<sup>-1</sup> at 532 nm, among the highest reported up-to-date for single-nanoribbon photodetectors. These findings can inspire the design of MoS<sub>2</sub> semiconductors with tunable geometries for efficient optoelectronic devices.

predicted to exhibit strikingly distinct functionalities from their 2D counterpart. Due to their high surface-to-volume ratios, the 1D semiconductor nanostructures have emerged as key components for various applications, including nanolasers,<sup>[1]</sup> light-emitting diodes,<sup>[2]</sup> and photodetectors.<sup>[3]</sup> In particular, photodetectors based on 1D semiconductor nanoribbons, including GaSe,<sup>[4]</sup> ZrGeTe,<sup>[3]</sup> with various bandgaps in the visible light spectral region and broad spectral responses, have been reported. Among 2D materials, transition metal dichalcogenides (TMDs), such as MoS<sub>2</sub>, have sparked a great interest due to the possibility of tailoring their electrical, optical, and magnetic properties via substitutional,<sup>[5]</sup> electrostatic doping,<sup>[6]</sup> and charge transfer.<sup>[7]</sup> The excellent photon absorption and emission of single-layer TMDs, fast photocurrent switching, and high photoresponsivity have sparked a great interest in realizing photodetectors,<sup>[8]</sup> light-emitting diodes,<sup>[9]</sup> and solar cells.<sup>[10]</sup> Recently, new exotic properties have been realized in TMDs with reduced


## 1. Introduction

One-dimensional (1D) semiconductor nanostructures, such as nanorods, nanowires, nanobelts, and nanoribbons, have been

dimensionality. WS<sub>2</sub> nanorods with merely broken symmetry have shown an enhanced shift current and bulk photovoltaic effect.<sup>[11]</sup> MoS<sub>2</sub> nanoribbons with S-terminated zigzag edges have been theoretically predicted to have high thermodynamic

G. Ghimire, R. K. Ulaganathan, D. I. Miakota, S. Canulescu  
Department of Electrical and Photonics Engineering  
Technical University of Denmark  
Roskilde 4000, Denmark  
E-mail: stec@fotonik.dtu.dk  
A. Tempez, M. Chaigneau  
Horiba France SAS  
Palaiseau 91120, France

O. Ilchenko  
Department of Health Technology Nanoprobes  
Technical University of Denmark  
Kongens Lyngby 2800, Denmark  
R. R. Unocic, D. B. Geohegan  
Center for Nanophase Materials Sciences and Materials Science and  
Technology Division  
Oak Ridge National Laboratory  
Oak Ridge, TN 37830, USA  
J. Heske, C. Xiang, T. Booth, P. Bøggild, K. S. Thygesen  
Department of Physics  
Technical University of Denmark  
Kongens Lyngby 2800, Denmark

 The ORCID identification number(s) for the author(s) of this article can be found under <https://doi.org/10.1002/adma.202302469>

© 2023 The Authors. Advanced Materials published by Wiley-VCH GmbH. This is an open access article under the terms of the Creative Commons Attribution-NonCommercial License, which permits use, distribution and reproduction in any medium, provided the original work is properly cited and is not used for commercial purposes.

DOI: 10.1002/adma.202302469

stability and edge-dependent characteristics, with armchair and zigzag edges exhibiting semiconducting and metallic character, respectively.<sup>[12,13]</sup> Moreover, the optical, electrical, magnetic, and catalytic properties of TMD nanoribbons can be modified in the presence of edge defects<sup>[14]</sup> by doping,<sup>[15]</sup> strain,<sup>[16]</sup> and strain-induced polarization.<sup>[17]</sup> Hence, exploring facile methods for the synthetic design of TMD nanoribbons with tailored dimensionality can open new avenues for realizing nanodevices with novel functionalities.

The MoS<sub>2</sub> nanoribbon geometry has been previously achieved using patterned templates or the focused ion beam milling method.<sup>[18,19]</sup> Alternatively, a bottom-up synthesis approach can be adopted based on vapor-liquid-solid (VLS) approach, which has been well established for the growth of various materials, including graphene<sup>[20]</sup> and GaSe nanoribbons.<sup>[21]</sup> Li et al. have demonstrated the growth of MoS<sub>2</sub> nanoribbons using Ni particles as promoters.<sup>[22]</sup> Wu et al. reported on the growth of MoS<sub>2</sub> nanoribbons on sapphire without catalysts.<sup>[23]</sup> In the VLS growth, the super-saturated liquid droplets are formed by a sodium chloride reaction with molybdenum oxide (MoO<sub>3</sub>).<sup>[24]</sup> Furthermore, the VLS method can be used for 1D growth because 1D nanostructures are favorable during the growth steps from super-saturated catalytic droplets. The substrate can also influence growth to a large extent, which is one inherent restriction of this approach. Similarly, Pho et al. have demonstrated molybdenum diselenide (MoSe<sub>2</sub>) nanoribbons by molecular beam epitaxy on highly aligned polycrystalline graphite.<sup>[25]</sup> Cheng et al. reported the growth of MoSe<sub>2</sub> nanoribbons using a patterned gold (Au-100) substrate.<sup>[26]</sup> Despite advances in synthetic methods, scarce reports on photodetectors based on TMD nanoribbon arrays have shown modest photodetectivity.<sup>[4,18]</sup>

We herein demonstrate an ultra-sensitive photodetector based on a single MoS<sub>2</sub> nanoribbon fabricated by a VLS process. Our approach involves the reaction between uniform oxide precursors grown by pulsed laser deposition (PLD) and NaF in an S-rich environment. The synthesis method yields high-quality MoS<sub>2</sub> nanostructures consisting of nanoribbons and 2D triangular crystals and aligned 3D crystals with either 3R or 2H stacking orientation. Controlling the growth parameters, namely temperature and oxide precursor thickness, allows MoS<sub>2</sub> nanoribbons to reach several micrometers in length and tens of nanometers in height. Moreover, the MoS<sub>2</sub> nanoribbons exhibit monolayer edges, as revealed by scanning electron microscopy (SEM), atomic force microscopy (AFM), and second harmonic generation (SHG). Tip-enhanced photoluminescence (TEPL) spectroscopy reveals distinct PL features originating from monolayer nanoribbons and 2D crystals, with nanoribbons exhibiting blue-shifted PL emission compared to 2D MoS<sub>2</sub> crystals, owing to the built-in local strain in the nanoribbon. In addition, we report on the first photodetector based on a single MoS<sub>2</sub> nanoribbon on rigid substrates (SiO<sub>2</sub>/Si). The response generated under illumination is orders of magnitude larger than other nanoribbon materials, owing to the high crystallinity of the MoS<sub>2</sub> nanostructures. Our findings underline the great promise of TMD-based nanoribbons for future applications in next-generation electronics and optoelectronic devices.

## 2. Results and Discussion

### 2.1. Synthesis of MoS<sub>2</sub> Nanoribbons

The MoS<sub>2</sub> nanoribbons were grown in a two-step process in which ultra-thin oxide films were sulfurized in the presence of alkali halide promoters. The role of alkali metal halides in promoting the unidirectional synthesis of MoS<sub>2</sub> nanoribbons from MoO<sub>3</sub> solid precursor has been discussed in our previous work.<sup>[27]</sup> Notably, without the alkali metal halide layer promoter (NaF), the oxide-to-sulfide conversion leads to quasi-continuous MoS<sub>2</sub> layers of quality like the conventional CVD process (see Figure S1, Supporting Information). Figure S2 (Supporting Information) describes the details of the synthesis process. Briefly, ultra-thin films of molybdenum oxide MoO<sub>x</sub> ( $2 < x < 3$ ) grown by PLD on c-plane sapphire serve as precursors.

PLD is a versatile tool that allows a broad tunability of the precursor uniformity, thickness, and stoichiometry, the latter by varying the oxygen content.<sup>[28,29]</sup> In the second step, the precursor oxide films coated with alkali metal halide (NaF) are sulfurized in an S-rich atmosphere. In contrast to the conventional CVD, our approach allows decoupling evaporation from the growth processes. At a low temperature (600 °C), the uniform MoO<sub>x</sub> precursor thin film reacts with NaF to form liquid Na–Mo–O phases, that is, Na<sub>2</sub>MoO<sub>4</sub> or Na<sub>2</sub>Mo<sub>2</sub>O<sub>7</sub>, and volatile molybdenum oxyhalides phases, such as NaMo<sub>2</sub>F<sub>2</sub>. The resulting products have much lower melting temperatures than starting solid-state precursors of MoO<sub>2</sub>, MoO<sub>3</sub>, or NaF (see Section 4 of Supporting Information for details). It is important to note that both liquid and gaseous precursors contribute to the growth of MoS<sub>2</sub>, from the liquid phase via the VLS process<sup>[27,30]</sup> and the gas phase via the vapor–solid mechanism process,<sup>[31,32]</sup> respectively. When introduced at a high temperature (800 °C), sulfur dissolves into the liquid droplet, forming MoS<sub>2</sub> nucleation sites via the VVS process. As MoS<sub>2</sub> continues to precipitate, the liquid droplet will crawl on the sapphire leading to unidirectional nanoribbon growth.<sup>[27,30]</sup> During the lateral expansion of the nanoribbons on sapphire, sulfur (predominantly thermally cracked S<sub>2</sub> molecules<sup>[33]</sup>) will continue to dissolve into the Na–Mo–O droplet, leading to the outgrowth of monolayer MoS<sub>2</sub>, and hence the formation of the monolayer edge of the nanoribbon. Indeed, a series of start/stop experiments, in which the synthesis was intentionally interrupted at the temperature range from 600 to 800 °C, reveals that the nanoribbons are already formed at 600 °C. Still, the monolayer edges are barely visible at low temperatures and very pronounced at 800 °C (Figure S6, Supporting Information). Last, the volatile gaseous precursors of NaMo<sub>2</sub>F<sub>2</sub> generated in the reaction will supply an increased concentration of the Mo precursor during the growth. Upon reaction with sulfur, they will facilitate the growth of single-layer (2D) and multilayer (3D) MoS<sub>2</sub> triangles.<sup>[32]</sup> The formation of 2D and 3D nanostructures will depend on the local concentration of the precursors, with a higher concentration resulting in a more favorable multilayer 3D growth. The formation of 2D and 3D nanostructures will depend on the local concentration of the precursor. As discussed later, the nanoribbons and 3D triangles feature monolayer edges, forming a monolayer–multilayer interface, enabling the formation of a junction due to the lateral change in thickness and, thus,

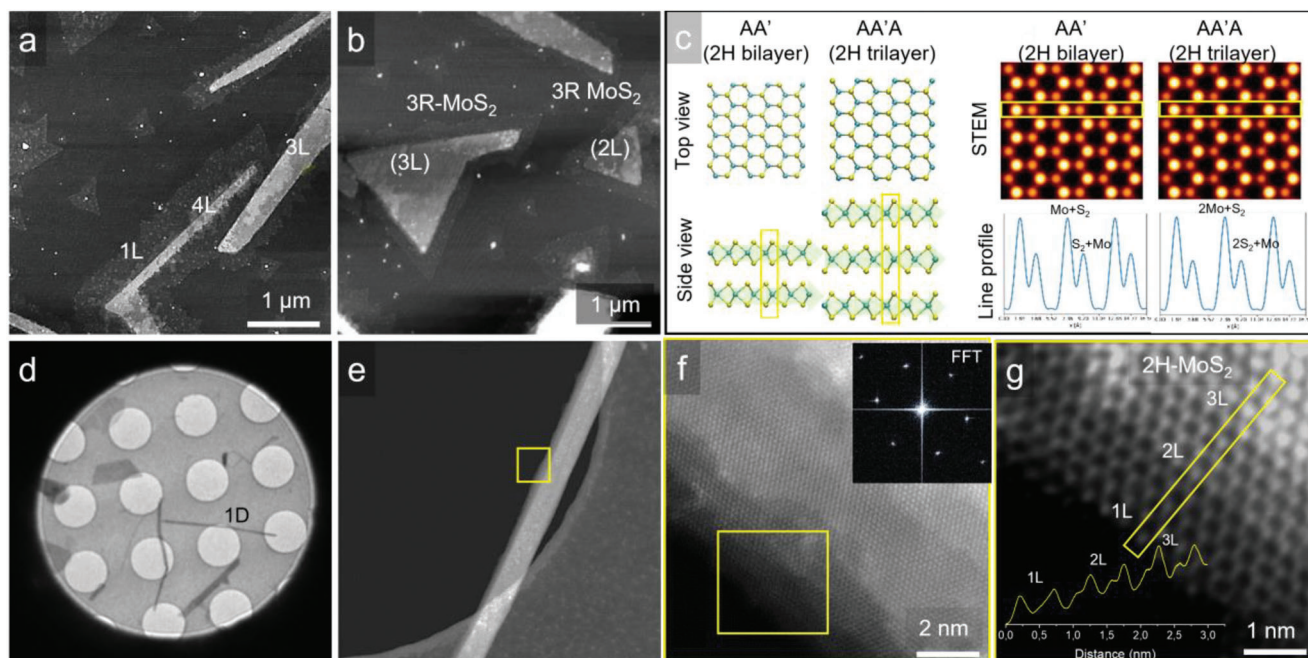


**Figure 1.** Morphology and atomic resolution images of the MoS<sub>2</sub> nanoribbons. a) AFM image of the as-grown multilayer nanoribbons with lengths up to 10 μm and single-layer nanoribbon edges. b) AFM image of the bilayer (2L) and trilayer (3L) MoS<sub>2</sub> triangular crystals with 3R stacking orientation. c) Relaxed atomic models of the 2H bilayer (AA' stacking) and trilayer (AA'A stacking) MoS<sub>2</sub>, with top and side views, respectively. Simulated STEM images of the 2L and 3L 2H-MoS<sub>2</sub> based on the theoretical relaxed structures with the same beam energy, convergence angle, and collection angles as in data acquisition. Line scans across the lattice points indicated by the overlaid rectangles. d) Low-magnification image of the nanoribbons transferred on the TEM grid. e–g) High-resolution ADF-STEM images of the multilayer nanoribbon. The inset in (f) shows the FFT spectrum of the STEM image. Experimental line profiles across the rectangle overlaid in (g) indicate a 2H stacking of the 2L and 3L MoS<sub>2</sub>.

bandgap. **Figure 1a** shows the AFM images of the MoS<sub>2</sub> nanoribbons on sapphire. The nanostructures are multilayer nanoribbons with a thickness ranging between 2 and 3 nm, corresponding to three (3L) and four layers (4L) MoS<sub>2</sub>, respectively. They have lengths of up to 10 μm and widths of up to 500 nm yielding length-to-width ratios of 20 (see Figures S3, S4, Supporting Information). Herein, we will refer to these nanostructures as nanoribbons to reflect their reduced dimensionality in one direction compared to the triangle-shaped crystals. Remarkably, the nanoribbons exhibit monolayer edges that extend over several hundred nanometers, as can be unambiguously distinguished in the AFM line profiles shown in Figure S5 (Supporting Information). The monolayer nanoribbon is a single-crystal film that emerged upon the coalescence of multiple adjacent MoS<sub>2</sub> domains, as indicated by the overlaid triangles in Figure 1b. Depending on the precise manner two MoS<sub>2</sub> domains merge, various types of grain boundaries consisting of 4|4, 5|7, 6|8, and 4|6 dislocation core structures can form, which have been predicted by previous theoretical studies to hamper the properties of devices.<sup>[34]</sup> Here, the zigzag edges with 60° angles imply that single-crystal monolayer nanoribbons are formed from highly-aligned MoS<sub>2</sub> domains with a 0° orientation angle. The multilayer nanoribbon core presumably drives the lateral growth of self-aligned nanoribbons.

Besides the structures, MoS<sub>2</sub> triangles were frequently observed on the c-plane sapphire substrate.<sup>[35]</sup> Figure 1c shows the AFM images of single layers and bi-, trilayer triangles with 2H stacking orientation, namely AA' and AA'A, respectively. Notably, various annotations are being used in the literature for the 2H

(space group P6<sub>3</sub>/mmc) and 3R (space group R3m) stacking prototypes of MoS<sub>2</sub><sup>[36,37]</sup>. Here, we adopt the spectroscopic notations defined in theoretical studies,<sup>[38,39]</sup> for which AA' reflects a 2H-MoS<sub>2</sub> bilayer with a 180° twist angle between layers, restoring the inversion symmetry. In contrast to single-layer 2H-MoS<sub>2</sub>, the 2H stacking orientation restores the inversion symmetry in bulk.<sup>[37]</sup> Hence, the symbol prime in the notation above designates a mirror symmetry. This is in strong contrast to the 3R-stacked MoS<sub>2</sub>, in which the layers share the same crystallographic orientation and shift relative to the bottom layer by  $\sqrt{3}a/3$  along the ZZ direction, leading to an ABC stacking order.

Next, the stacking order of the multilayer MoS<sub>2</sub> nanoribbons was explored using atomic resolution annular dark field (ADF) imaging on an aberration-corrected scanning transmission electron microscope (STEM). For this purpose, the as-grown specimens were transferred onto a TEM grid (see Experimental Section and Figure 1d,e). The image intensity is proportional to the number of layers, providing an easy and accurate way to measure the thickness of MoS<sub>2</sub> layers, as demonstrated previously for PLD-grown films MoS<sub>2</sub>.<sup>[34]</sup> Figure 1e–h shows the ADF-STEM images of the multilayer nanoribbons. The layered structure is evidenced in the atomic resolution image shown in Figure 1g. A magnified view over the edge of the MoS<sub>2</sub> nanoribbon reveals an image intensity contrast due to a change in the number of layers. The atom-by-atom analysis of the image intensity enables us to identify the intensity profiles from 1L, 2L, and 3L MoS<sub>2</sub>. The fast Fourier transform (FFT) of the multilayer nanoribbon shown in the inset of Figure 1g illustrates one set of sixfold diffraction

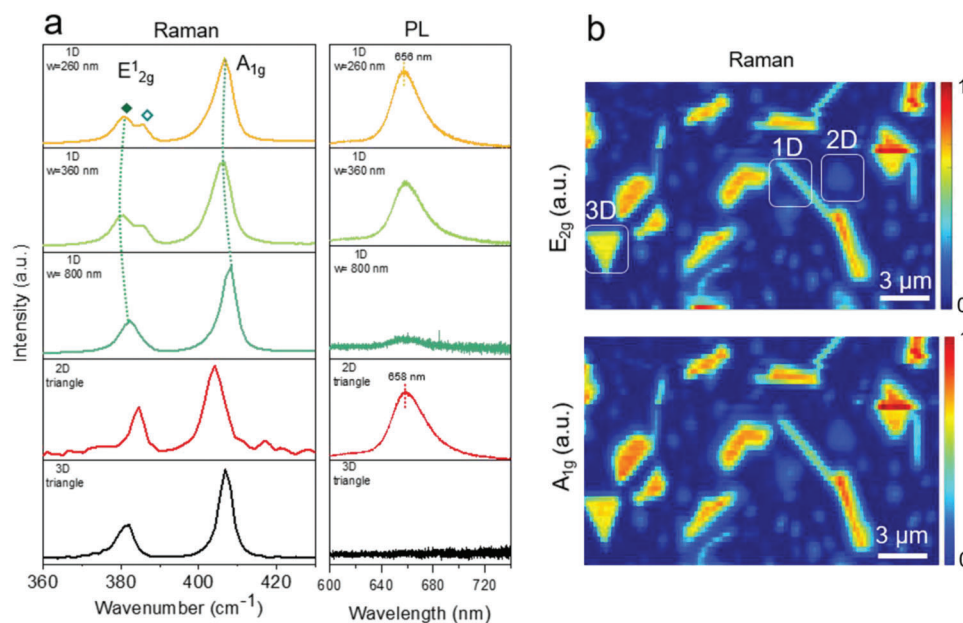


**Figure 2.** Optical properties of the MoS<sub>2</sub> nanostructures with distinct dimensions. a) Raman and PL spectra of triangle-shaped monolayer (2D), nanoribbons with core widths ( $w$ ) of 260, 360, and 800 nm, and multilayer triangular MoS<sub>2</sub> crystals (3D). The full and empty diamond symbols denote the Raman peaks of the core and monolayer nanoribbon, respectively. b) Raman maps show the intensity of the  $E_{2g}^1$  peak (top image) and the  $A_{1g}$  peak (bottom image). The parameter  $w$  indicates the width of the multilayer nanoribbon core and excludes the contribution from the monolayer nanoribbon edge.

points associated with the hexagonal crystal structure, which indicates a high-quality epitaxial multilayer MoS<sub>2</sub> nanoribbon with either 2H or 3H stacking orientation. To correctly assess the stacking order of the multilayer nanoribbons, we performed first-principles calculations based on density functional theory (DFT). The 3R stacking registry can be ruled out due to the absence of the S<sub>2</sub> atoms in the honeycomb lattice (see simulated STEM images in Figure S7, Supporting Information). The atomic structures of the 2H AA' bilayer and AA'A trilayer are shown in Figure 1d with the relaxed structural models extracted from the DFT calculations. The simulated STEM images show distinct intensities at two sublattices, that is, Mo + S<sub>2</sub>, S<sub>2</sub> + Mo for bilayer MoS<sub>2</sub> (AA' stacking) and 2Mo + S<sub>2</sub>, 2S<sub>2</sub> + Mo for trilayer MoS<sub>2</sub> (AA'A stacking). The line scans across two inequivalent lattice points in the simulated STEM images reveal an intensity ratio difference of  $\approx 8\%$  between the 2H-bilayer and trilayer MoS<sub>2</sub>. The experimental line profiles shown in Figure 1g agree with the theoretically calculated profiles in Figure 1c. However, we note that the experimental images are less sharp than the simulated ones due to electron probe tailing and drifting effects during STEM imaging. Last, while the 2H stacking prevails over the 3R stacking, we cannot exclude the presence of both low-energy stacking sequences in our samples.<sup>[39]</sup>

## 2.2. Optical Properties of the MoS<sub>2</sub> Nanoribbon

We then explored the optical properties of our experimentally synthesized MoS<sub>2</sub> nanostructures with distinct crystal shapes using Raman and photoluminescence (PL) spectroscopy. Figure 2 shows representative Raman spectra of the nanoribbons with widths ranging from 260 to 800 nm and single- and multilayer tri-

angles. The width of the multilayer nanoribbon (annotated with the symbol  $w$  in Figure 2a) excludes the contribution from the monolayer edge. The Raman spectrum of the 2D triangle MoS<sub>2</sub> shows two peaks at 384.2 and 404.2  $\text{cm}^{-1}$ , attributed to the in-plane  $E_{2g}^1$  and out-of-plane  $A_{1g}$  lattice vibrations of MoS<sub>2</sub>, respectively. The estimated peak difference of 20  $\text{cm}^{-1}$  agrees with previous reports on exfoliated or CVD monolayers.<sup>[40]</sup> For the 3D crystals, the Raman spectroscopic features of 3R-oriented crystals are different from those of the conventional 2H counterparts due to a more significant reduction in the van der Waals gap, which results in a change in the phonon frequencies. Interestingly, we find that the peak positions of the 3R crystals match well those of multilayer triangular crystals with 3R stacking sequence (AA(A' . . .)-type stacking reported in previous studies.<sup>[37]</sup> Hence, the peak position and peak difference can be used to confirm the 3R stacking orientation of the 3D triangular crystals.

Remarkably, the nanoribbons exhibit strikingly distinct Raman features compared to the 2D and 3D structures. The  $A_{1g}$  peak blue shifts by more than 4  $\text{cm}^{-1}$  compared to the 2D triangle due to interlayer coupling, while the  $E_{2g}$  peak redshifts by more than 2  $\text{cm}^{-1}$  from the dielectric screening. Moreover, a pronounced splitting of the  $E_{2g}^1$  and  $A_{1g}$  Raman modes is observed, particularly for the narrow nanoribbons. The splitting vanishes for the structures with widths of 800 nm and above. These Raman features have not been observed previously and, in sharp contrast to the scenario of strained monolayer MoS<sub>2</sub>, lattice deformation (strain) and charge transfer (doping) are unlikely to be the sole factors in multilayer nanoribbons. We hypothesize that the pronounced peak splitting is a dual contribution from the multilayer nanoribbon core and monolayer edge. Indeed, the laser spot size used to acquire Raman spectra was estimated to be  $\approx 720$  nm ( $\lambda = 532$  nm,  $M^2 = 1$ ,  $NA = 0.9$ ), meaning that the entire struc-

ture (core and edge) is probed in the case of the narrow nanoribbons. However, this is not the case for the nanoribbons 800 nm wide, in which the laser beam is smaller than the width of the multilayer nanoribbons. The deconvolution of the Raman spectra of the nanoribbons enables us to identify low-frequency  $E_{2g}^2$  mode at 380.6 and 384.5  $\text{cm}^{-1}$  and higher frequency modes at 403 and 405.4  $\text{cm}^{-1}$  for the single layer and 260 nm-wide multilayer nanoribbons, respectively. This corresponds to a peak difference of 18.5 and 24.8  $\text{cm}^{-1}$ , respectively. The peak fitting results are presented in Note S6 (Supporting Information). Regardless of the aforementioned contributions to the Raman spectra, the  $E_{2g}^1$  and  $A_{1g}$  Raman modes of the nanoribbon core blueshift with decreasing width owing to strain in the nanoribbons. The shift does not appear to vary linearly with the nanoribbon width (see dotted lines in Figure 2a), indicating that the built-in strain is more pronounced for the narrow nanostructures than the broad counterparts. The Raman intensity maps provide a visual distribution of the nanostructures on sapphire. The overlaid rectangles in Figure 2b highlight the low-intensity region associated with single-layer  $\text{MoS}_2$  and the brighter regions of the 3D structures. The edges of the nanostructures have a lower intensity than their inner structures, which is consistent with single-layer nanoribbon edges observed in the SEM and AFM images.

The PL spectra of as-grown specimens were measured at the same locations as the Raman spectra shown in Figure 2a, right-hand plot. The PL peak of the 2D triangle is located at  $\approx 658$  nm (1.884 eV), corresponding to the A direct excitonic transition in  $\text{MoS}_2$ , which is in good agreement with the PL spectra of the quasi-continuous  $\text{MoS}_2$  layer (Figure S1, Supporting Information). No PL emission can be observed from the 3D triangle-shaped structures, consistent with the indirect band gap semiconductor for the multilayer structure. This strongly contrasts with the multilayer nanoribbons, for which the PL emission is comparable to a single-layer  $\text{MoS}_2$ . We note that the PL peak blue shifts from 658 nm (1.884 eV) to 655 nm (1.896 eV) correspond to a small energy shift of 27 meV, likely due to intrinsic strain in the as-grown nanostructures.<sup>[41]</sup>

### 2.3. Nanoscale Imaging of the $\text{MoS}_2$ Nanoribbons using Tip-Enhanced PL Spectroscopy

As discussed above, the multilayer  $\text{MoS}_2$  nanoribbons exhibit noticeable PL emission, which is not expected for multilayer structures. The narrow nanoribbons can reach a thickness of 15 nm and are thicker than the broad nanoribbons (Figure S4, Supporting Information), indicating local variations in the precursor composition during growth. Given the nanoribbon bulk structure, the enhanced PL emission is presumably attributed to the monolayer edges. However, far-field spectroscopy only provides a macroscale picture of the emission of the structures. Here we have performed TEPL with the optical excitation confined to a few nanometers to enable mapping the spatial distribution of exciton emission from the core and edge of the nanoribbons. The correlated AFM and Kelvin probe force microscopy (KPFM) surface scans were used to localize and directly visualize the as-grown nanostructures, as shown in Figure 3a,b. Moreover, the KPFM image intensity is directly related to the work function of the material under study, enabling accurate identification of

the number of layers via quantitative image intensity analysis. A careful inspection of the KPFM image reveals that the region of the nanoribbon appears darker than the underlying sapphire substrate, and this can be explained due to a higher work function of  $\text{MoS}_2$  compared to sapphire. KPFM mapping enables us to resolve the zigzag edges of the monolayer nanoribbon edge while the nanoribbon core is barely visible. This agrees with previous work, which indicates a difference in work function between single- and multilayer of 70 meV.<sup>[42]</sup> Small dots on the surface of the nanoribbon, clearly distinguishable in the AFM image, have a different color contrast (hence work function) than the underneath  $\text{MoS}_2$  layer in the KPFM scan and can probably be due to the oxidation of the top layer. Here, KPFM is only used as a qualitative tool, and a direct determination of the work function of the nanoribbons is beyond the scope of the work. The TEPL map acquired using a 532 nm laser reveals a pronounced emission from the nanoribbon edge (blue area in Figure 3c). In contrast, the nanoribbon core appears dark due to an indirect band gap of the thick  $\text{MoS}_2$  structure. The integrated PL spectra from regions marked in Figure 3c are plotted as in Figure 3d. The excitonic emission from the 2D  $\text{MoS}_2$  flake (located at the left of the TEPL image) is slightly red-shifted compared to the single-layer nanoribbon, in good agreement with the far-field spectroscopy results, suggesting that local strain can play a role in the observed shift. Maps of the integrated PL peak position and intensity reveal small spatial variations across the nanoribbon's edge (Figure S8, Supporting Information). Variation in the PL intensity response of the nanoribbon is not specific to the location of edges, and systematic changes have also been observed in single crystals. Here, we attribute these changes to the strain accumulated in the material during the growth because there is a difference between the thermal expansion coefficient of  $\text{MoS}_2$  and sapphire. An enhanced exciton emission at the nanoribbon edges has also been observed on other nanostructures (see Figure S9, Supporting Information).

### 2.4. SHG of $\text{MoS}_2$ Nanoribbons

The lack of inversion symmetry in TMDs reflects the second-order nonlinear optical response of vdW materials.<sup>[43]</sup> Hence, SHG can be readily exploited to identify the crystal symmetry in layered TMDs.<sup>[44]</sup> The origins of the strong nonlinear optical response in single-layer TMDs have been extensively discussed in the literature.<sup>[36,39,44,45]</sup> Monolayers 2H- $\text{MoS}_2$  exhibit an SHG response due to a lack of inversion symmetry. On the other hand, multilayers of  $\text{MoS}_2$  can have distinct symmetry properties. In the AA(A' . . .)-type stacked  $\text{MoS}_2$  (2H), the most thermodynamically favorable prototype, the SHG intensity of the Nth-layered  $\text{MoS}_2$  strongly depends on the layer number. Odd-numbered layers are non-centrosymmetric, retaining a net dipole, whereas even-numbered layers do not. In contrast, 3R- $\text{MoS}_2$  belongs to a centrosymmetric space group, and the non-inversion symmetry is preserved in bulk. For the non-centrosymmetric 3R crystal of  $\text{MoS}_2$ , a quadratic dependence of the SHG intensity on the number of layers has been predicted due to constructive interference of the nonlinear dipoles.<sup>[46]</sup>

Figure 3 shows the SHG image of  $\text{MoS}_2$  nanostructures with distinct dimensionalities acquired at 785 nm. Here, the light is

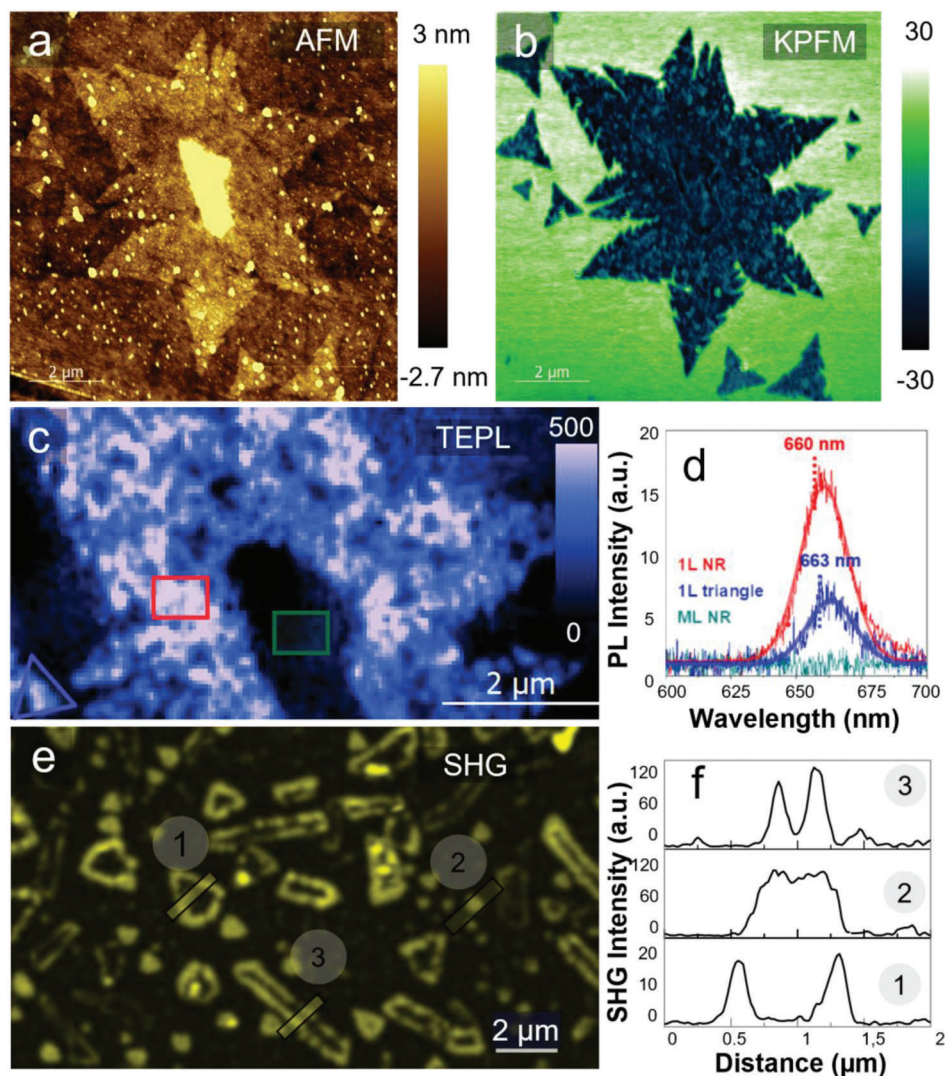


**Figure 3.** Nano- and micro-scale mapping of the MoS<sub>2</sub> nanostructures. a) AFM topographic image of a small MoS<sub>2</sub> nanoribbon. b) Contact potential difference from frequency-modulated KPFM. c) TEPL map of the MoS<sub>2</sub> nanoribbon acquired with 532 nm excitation laser. d) PL spectra averaged from the rectangles overlaid in (c) show the exciton emission from a monolayer nanoribbon (1L NR), monolayer triangle (1L triangle), and multilayer nanoribbon (ML NR). e) SHG image of distinct MoS<sub>2</sub> nanostructures: 1) multilayer 3D triangle, 2) 2D MoS<sub>2</sub>, and 3) multilayer nanoribbon. f) Line profiles across the three distinct MoS<sub>2</sub> nanostructures, as shown by the overlaid rectangles in (e).

incident on the surface, and the integrated second harmonic radiation is collected. Small triangles with a uniform SHG intensity can be identified, likely attributed to the single layer of 2H-MoS<sub>2</sub> (point 2 in Figure 3e). Surprisingly, the SHG map reveals edge-enhanced SHG for the nanoribbons and 3D multilayer crystals (points 1 and 3 in Figure 3e).

The intensity profiles show that the SHG intensities of the MoS<sub>2</sub> nanoribbons and 3D triangles of MoS<sub>2</sub> rise abruptly at the edges but decrease much slower toward the inner parts of the nanostructures (Figure 3f). Sometimes, the intensity drop does not approach the baseline, particularly for the MoS<sub>2</sub> nanoribbons (plot 3 in Figure 3f). The edge-enhanced SHG was observed at the excitation wavelengths of 825, 875, and 1032 nm, with a significantly reduced SHG intensity for the latter (see Figure S10, Supporting Information). The edge-enhanced SHG in nanoribbons and 3D structures can be attributed to their corresponding mono-

layer edges, which lack inversion symmetry. The low SHG intensity in the inner structures suggests that the given nanostructures have a 2H stacking or similar, which is centrosymmetric.<sup>[39,47]</sup> The edge-enhanced SHG was previously attributed to distinct edge states due to the translational symmetry breaking in monolayer MoS<sub>2</sub>.<sup>[43]</sup> However, the photon energy of 1.57 eV (785 nm) is far from the resonance wavelength of 0.95 eV (1300 nm), at which a pronounced edge-enhancement SHG was observed. Hence, our findings differ significantly from those described earlier,<sup>[43,48]</sup> and the enhanced SHG intensity can likely be associated with the non-centrosymmetric monolayer edges. Here, an additional factor that can contribute to the edge-enhanced SHG is the broken crystal symmetry due to band bending, in analogy with band bending-induced SHG in non-centrosymmetric GaAs.<sup>[49]</sup> Indeed, one can recognize that the edges of the nanostructures form a sharp monolayer–multilayer MoS<sub>2</sub> homojunction enabled

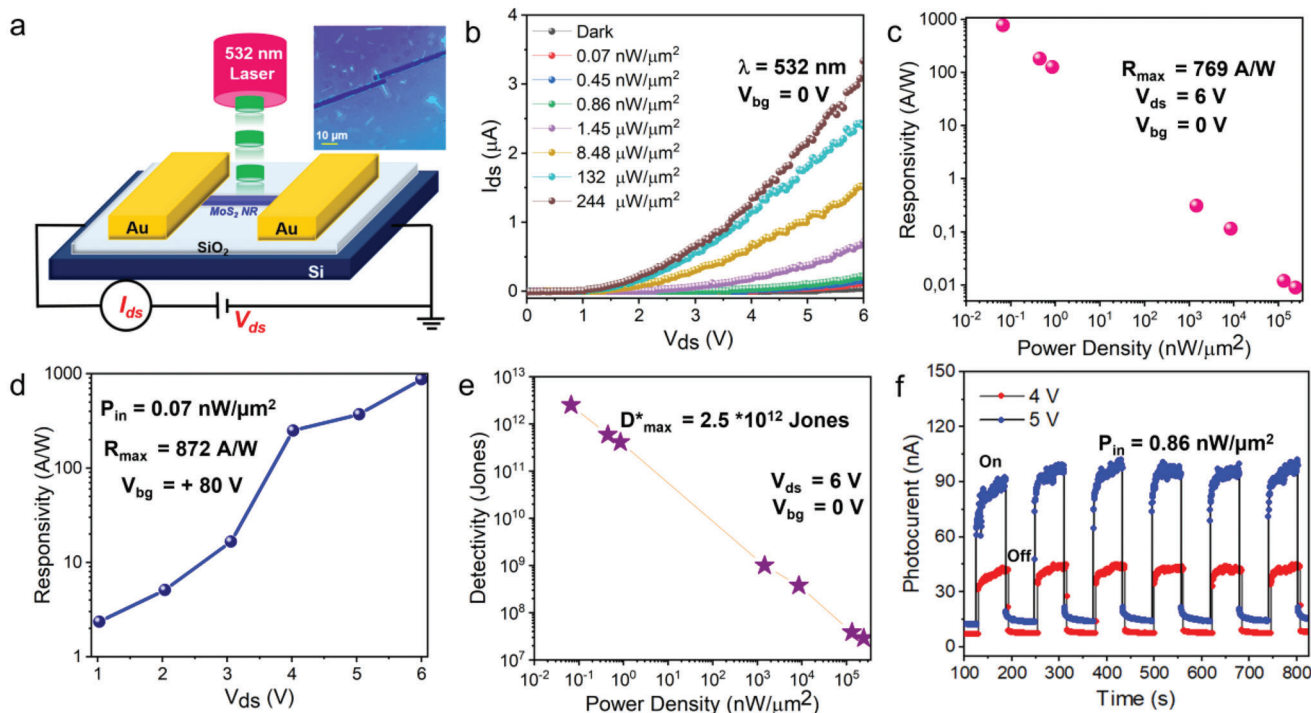


**Figure 4.** Single nanoribbon MoS<sub>2</sub> photodetector. a) Schematic of the MoS<sub>2</sub> nanoribbon device on SiO<sub>2</sub>/Si substrate with 532 nm laser beam shining on the device channel. The inset shows an optical image of the device. b) The output  $I_{ds}$ - $V_{ds}$  characteristic of the device in the dark and under illumination at various light intensities. c) The extracted responsivity of a single MoS<sub>2</sub> nanoribbon as a function of illumination power density. The device exhibits a maximum responsivity of 769 A W<sup>-1</sup> at the power density of 0.07 nW μm<sup>-2</sup>,  $V_{ds}$  = 6 V, and  $V_{bg}$  = 0 V. d) Gating responsivity as a function of  $V_{ds}$  at the back gate voltage of +80 V. The responsivity increases with  $V_{ds}$  and reaches the maximum value of 872 A W<sup>-1</sup> for  $V_{ds}$  = 6 V. e) The detectivity of the single MoS<sub>2</sub> nanoribbon was measured at  $V_{ds}$  = 6 V and  $V_{bg}$  = 0 V. f) Time-resolved photoswitching response of the device at  $V_{ds}$  of 4 and 5 V.

by the sharp modulation in the MoS<sub>2</sub> thickness (hence the band gap) at the interface. This leads to an interfacial band bending and a strong built-in electric field, and the magnitude of the band bending will depend on the carrier concentration of TMDs. Since the presence of single-layer edges leads to the formation of a lateral homojunction, the two effects leading to edge-enhanced SHG cannot be decoupled. Last, one can observe that the SHG intensity is not entirely uniform along the edges of the 3D nanostructures and nanoribbons, with apparent variations in intensity present. As discussed earlier, according to the Raman spectra, the nanoribbons have extended monolayer edges that feature a built-in strain. The strain can lift the crystal symmetry and enhance the SHG response in TMDs.<sup>[50,51]</sup> Hence, the local built-in strain is likely responsible for the variation of the SHG intensity along the edges of the nanoribbons.

## 2.5. MoS<sub>2</sub> Photodetectors

To assess the electrical performance of MoS<sub>2</sub> nanoribbons, we have fabricated a photodetector device based on a single MoS<sub>2</sub> nanoribbon. The photogenerated current under 532 nm illumination was measured by recording the source-drain current ( $I_{ds}$ ) as a function of the applied voltage ( $V_{ds}$ ). **Figure 4a** illustrates the schematic of a MoS<sub>2</sub> nanoribbon photodetector on a SiO<sub>2</sub> (300 nm)/Si substrate. The inset of **Figure 4a** shows an optical image of the single MoS<sub>2</sub> nanoribbon device. Here, Cr/Au lines

were used as source and drain contacts, with a spatial separation of 3 μm. As detailed in the device fabrication section, the metal contacts were deposited on top of the MoS<sub>2</sub> nanoribbon by standard photolithography. The  $I_{ds}$ - $V_{ds}$  characteristics of the MoS<sub>2</sub> nanoribbon in the dark and under illumination at 532 nm are shown in **Figure 4b**. One can observe an almost 10<sup>3</sup> times increase in photocurrent with increasing power density from 0.07 nW μm<sup>-2</sup> to 244 μW μm<sup>-2</sup>, indicating that the photodetector is highly sensitive to visible light. Indeed, at 244 μW μm<sup>-2</sup>, the photocurrent in the MoS<sub>2</sub> nanoribbon channel reaches ≈6 μA ( $V_{ds}$  = 6 V), which is three orders of magnitudes higher than the dark current (6 nA) at the same applied voltage. Next, we plot the photocurrent ( $I_{ph}$ ) by deducting the ( $I_{ds}$ ) obtained in the dark ( $I_{dark}$ ) from that under illumination ( $I_{light}$ ) as a function of incident power density. The  $I_{ph}$  increases sub-linearly with light intensity, as shown in **Figure S11** (Supporting Information). From the output characteristic curves (**Figure 4b**; **Figure S12**, Supporting Information), the critical figure of merits, that is, responsivity and specific detectivity, were evaluated for the single nanoribbon MoS<sub>2</sub> device. Responsivity ( $R_{\lambda}$ ) is the photocurrent produced per incident light on an active illuminated area. It is expressed by  $R_{\lambda} = (I_{ph})/(PS)$ , where  $I_{ph}$  is the photocurrent,  $P$  is the incident light density, and  $S$  is the illuminated channel area. The effective device area was estimated through the cross-sectional area of MoS<sub>2</sub> nanoribbon, which can be expressed as  $S = L \times w$ , where  $L$  is the length of the nanoribbon channel (3 μm), and  $w$  is the width of the nanoribbon (500 nm). **Figure 4c** shows the

photoresponsivity of a single MoS<sub>2</sub> nanoribbon as a function of incident power ranging from 0.07 nW μm<sup>-2</sup> to 244 μW μm<sup>-2</sup> at a fixed applied voltage and without back-gate voltage ( $V_{ds} = 6$  V,  $V_{bg} = 0$  V). At a low illumination of 0.07 nW μm<sup>-2</sup>, the device exhibits a remarkably high  $R_A$  of ≈769 A W<sup>-1</sup>. This value is 10<sup>4</sup> times higher than one of the multi-nanoribbon MoS<sub>2</sub> photodetectors (45 mA W<sup>-1</sup>),<sup>[18]</sup> several orders larger than graphene and GaSe nanoribbon devices.<sup>[21]</sup> The responsivity decreases with increasing effective illumination intensity due to the saturation of trap states at the MoS<sub>2</sub>/SiO<sub>2</sub> interface.<sup>[52]</sup> Moreover, we observe a small increase in the drain current with the applied gate voltage, that is, from 124 nA ( $V_{bg} = 0$  V) to 150 nA ( $V_{bg} = 80$  V) (Figure S12, Supporting Information). One can note that the  $V_{bg}$  dependence on the photocurrent magnitude is significantly lower than in previous literature reports on MoS<sub>2</sub> devices.<sup>[18,53]</sup> The responsivity of the MoS<sub>2</sub> nanoribbon channel at  $V_{bg} = 80$  V rises substantially from 769 to 872 A W<sup>-1</sup> (Figure 4d).

Another figure of merit, that is, the specific detectivity ( $D^*$ ), indicates the device's capability to identify weak optical signals is expressed by  $D^* = RS^{1/2}/(2eI_{dark})^{1/2}$ . The calculated  $D^*$  of our device is  $2.5 \times 10^{12}$  Jones at  $V_{ds} = 6$  V and  $V_{bg} = 0$  V, as shown in Figure 4e. The temporal photoresponse ( $I_{ds}-t$ ) and switching stability of the single MoS<sub>2</sub> nanoribbon in response to light illumination were conducted. The  $I_{ds}-t$  curve was recorded by illuminating the MoS<sub>2</sub> nanoribbon device using a 532 nm laser with a continuous ON/OFF cycle under different ( $V_{ds}$  of 4 and 5 V) and various illuminations, as shown in Figure 4f and Figure S11 (Supporting Information). At first, with  $V_{ds}$  of 4 V and light intensity of 0.86 nW μm<sup>-2</sup>, the device shows a sharp rise in photocurrent under laser ON condition, followed by a sudden drop and slower relaxation in the laser OFF state. This ON/OFF cycle is continued for several cycles. The reproducibility of consecutive switching ON/OFF cycles confirms the device's robustness and stability. At higher  $V_{ds}$  of 5 V, the same trend was noted with a slight increase in the photocurrent, which further proves the reliability of our MoS<sub>2</sub> nanoribbon device (Figure 4f). In addition, the ON-OFF measurement was carried out for different powers at constant ( $V_{ds}$ ) = 1 V, demonstrating the photocurrent's step-wise increase with increasing illumination (Figure S11, Supporting Information).

Under equilibrium, without an external bias ( $V_g = 0$ ,  $V_{ds} = 0$ ), the distribution of charge defects upon illumination is expected to be uniform throughout the nanoribbon core. For simplicity, we exclude the contribution of the nanoribbon edge. As mentioned above, the saturation of trap states occurs at higher illumination, as reflected in the photoresponsivity drop with increasing light intensity (Figure 4c). Under applied voltage ( $V_{ds} > 0$ ), the photogenerated carriers are efficiently swept out under the electric field toward the electrodes. This slowly empties the trap states,<sup>[52]</sup> leading to a significant increase in photocurrent with increasing  $V_{ds}$  and more efficiently at higher illumination (Figure 4c). The nanoribbon width comparable to the wavelength of light may lead to increased light-matter interaction, thereby increasing photocurrent.<sup>[18]</sup> The high photoresponse and detectivity could also be attributed to the high crystallinity of the as-grown nanoribbons. Moreover, one cannot exclude the role of the monolayer-multilayer homojunction on the overall increase in the photocurrent of the nanoribbon device. The alignment of the Fermi level at the junction leads to the diffusion of electrons

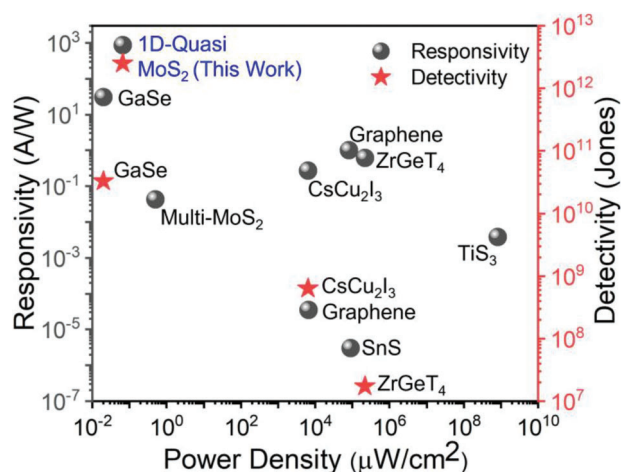


**Figure 5.** Overview of various nanoribbon devices' responsivities and detectivities versus power density. Reference data are taken from the literature for SnS,<sup>[54]</sup> graphene,<sup>[20]</sup> TiS<sub>3</sub>,<sup>[55]</sup> multi-MoS<sub>2</sub>,<sup>[18]</sup> ZnSe/Si,<sup>[56]</sup> CsCu<sub>2</sub>I<sub>3</sub>,<sup>[57]</sup> ZrGeTe<sub>4</sub>,<sup>[3]</sup> graphene and reduced oxide graphene,<sup>[58]</sup> GaSe.<sup>[21]</sup>

from the monolayer nanoribbon to the nanoribbon core and the accumulation of electrons at the junction, likely resulting in enhanced conductivity along the interface. The band bending at the nanoribbon edge induces a built-in electric field, which can efficiently dissociate excitons and enhance the photocurrent. One can recognize that, given our device geometry, the built-in electric field is perpendicular to the current of the nanoribbon channel and cannot effectively sweep out photogenerated carriers to the contacts. Hence, a  $V_{ds} > 0$  V bias is required to produce photocurrent in the circuit.

Next, we compare the detectivity and responsivity in our MoS<sub>2</sub> nanoribbon with those reported for similar devices based on nanoribbons. Figure 5 shows the responsivity (A W<sup>-1</sup>) and detectivity (Jones) as a function of power density (μW cm<sup>-2</sup>). Table S2 (Supporting Information) file also gives an overall comparison. Table S3 (Supporting Information) file compares the overall performance of the single-nanoribbon photodetector with other devices based on TMDs. Data for other materials are taken from the literature and correspond to figures of merits of other nanoribbon-based devices, that is, SnS,<sup>[54]</sup> graphene,<sup>[20]</sup> TiS<sub>3</sub>,<sup>[55]</sup> multi-MoS<sub>2</sub>,<sup>[18]</sup> ZnSe/Si,<sup>[56]</sup> CsCu<sub>2</sub>I<sub>3</sub>,<sup>[57]</sup> ZrGeTe<sub>4</sub>,<sup>[3]</sup> graphene and reduced oxide graphene,<sup>[58]</sup> GaSe.<sup>[21]</sup> The attained values are better than any other nanoribbon devices reported up to date and comparable to the commercially available Ge (10<sup>11</sup> Jones) and Si (10<sup>12</sup> Jones)-based photodetectors.<sup>[59]</sup>

### 3. Conclusion

In summary, we have demonstrated the growth of the highly crystalline multilayer (ML) MoS<sub>2</sub> nanoribbons with the assistance of NaF as a promotor. The NaF alkali metal halide plays a crucial role in forming multilayer nanoribbons and 3D stacked MoS<sub>2</sub> crystals, and in the absence of promoters, quasi-continuous MoS<sub>2</sub> layers are obtained. The MoS<sub>2</sub> nanoribbons exhibit distinct monolayer (1L) edges forming 1L-ML lateral homojunction. Due to edge defects and strain, the 1L edges of the nanoribbons



exhibit Raman and PL features distinct from those of a 2D MoS<sub>2</sub> triangle. A splitting of the Raman spectra was observed in the MoS<sub>2</sub> nanoribbons arising from distinct contributions from the 1L edges and ML core, which become more pronounced with the reduced width of the nanoribbon. Multiphoton microscopy reveals a greatly enhanced optical SHG from the 1L edges of the nanostructures, likely arising due to a non-centrosymmetric 1L and/or symmetry breaking at the surface. Moreover, we report on a high-performance single-nanoribbon MoS<sub>2</sub> photodetector a remarkable responsivity of  $7.69 \times 10^2 \text{ A W}^{-1}$  and measured specific detectivity of  $2.5 \times 10^{10}$  Jones at  $V_{\text{bg}} = 0 \text{ V}$ , superior to previously reported nanoribbon-based photodetectors. From a broader perspective, this work demonstrates a simple optoelectronic device architecture that can be applied to other TMDs to achieve high responsivity and detectivity and which features a 1L/ML junction intrinsic to the synthesis process and does not involve top-down fabrication techniques, such as laser thinning or layer-by-layer etching, that are amenable to generating intrinsic defects.

#### 4. Experimental Section

The precursor oxides were grown by laser ablation of a one-inch MoO<sub>3</sub> target (99.95% purity, from Testbourne Ltd.) in Ar at a pressure of 0.1 mbar. The target was ablated using a 248 nm KrF excimer laser operating at 1 Hz. The target-to-substrate distance was 7 cm. Before deposition, the vacuum chamber was pumped down to  $6 \times 10^{-7}$  mbar base pressure, and the target was pre-ablated using 60 laser pulses. All experiments maintained the laser fluence on the target at  $2 \text{ J cm}^{-2}$ . The films were grown on (0001) Al<sub>2</sub>O<sub>3</sub> substrates at a temperature of 700 °C using several laser shots varying from 5 to 20 pulses.

The 20 nm-thick NaF layer was deposited on top of the oxide precursors by thermal evaporation of NaF powder (99.9% purity, Sigma Aldrich) in a high vacuum at a pressure of  $6 \times 10^{-6}$  mbar. The depositions were done in an evaporation chamber from Univex 250 Oerlikon. The thickness of the NaF layers was estimated using an evaporation rate of  $0.3 \text{ \AA s}^{-1}$ .

The high-temperature growth of MoS<sub>2</sub> was carried out in a compact furnace, type OTF-1200X-4-NW-UL, from MTI Corporation. First, the precursor films were placed on a ceramic plate and loaded in the middle of the quartz tube of 4 inches outside diameter. An alumina ceramic boat containing sulfur flakes (1.5 g, purity 99.99, from Sigma Aldrich) was placed outside the central heating zone of the furnace and heated independently using an external heater. The distance between the ceramic boat and the samples was 28 cm. Before sulfurization, the quartz tube was evacuated to  $1.6 \times 10^{-3}$  mbar and filled with Ar-5% H<sub>2</sub> to 650 mbar to remove residual gases. After repeating the flushing cycle five times, the furnace was heated to 800 °C at a rate of 25 °C per min. The sulfurization process took place at 800 °C for 10 min. When the furnace reached 800 °C, the external heating zone containing the sulfur boat reached a temperature of 230 °C. When the growth was terminated, the system was cooled down at a rate of 20 °C min<sup>-1</sup> to 600 °C and then allowed to cool naturally to room temperature. A constant Ar-5% H<sub>2</sub> gas flow rate of 100 sccm was maintained throughout the process.

Raman and PL spectra were collected using a home-built Raman confocal spectroscopy setup using a 532 nm excitation laser. The spectrometer was a Spectra Pro HRS-750 scanning monochromator from Princeton Instruments equipped with three gratings of 300, 1200, and 1800 gr mm<sup>-1</sup> and a cryogenically-cooled, ultra-low noise Pylon CCD camera, type PyLoN:100BR. The wavelength calibration was carried out using an Ar-Ne light source mounted directly to the entrance slit of the spectrometer. The spectrometer resolution was 1 cm<sup>-1</sup>. Raman and PL spectra were collected using 300 and 1800 gr mm<sup>-1</sup>, respectively, and the laser power was kept below one mW to prevent samples from overheating. Leica TCS SP8 CARS microscope (Leica, Germany) was used for SHG imaging of MoS<sub>2</sub>

nanostructures. The system was equipped with a Pico Emerald laser (APE, Germany), where the Stokes laser wavelength was fixed at 1032.4 nm, and the pump laser was tunable in the range of 700–990 nm. Both lasers had a pulse duration of 2 ps with a repetition rate of 80 MHz. SHG images were carried out versus pump laser wavelength being tuned to 700, 750, 800 and 850, and 900 nm. Laser power was varied in a range from 12 to 25 mW. Stokes laser at wavelength 1032.4 nm was set to 25 mW of laser power at the sample. The specimens were illuminated through an objective lens with a magnification of 100× (Zeiss Objective EC Epiplan-Apochromat 100x/0.95 HD DIC M27), resulting in a diffraction-limited spot size with a full width of half maximum of  $\approx 380\text{--}520 \text{ nm}$  (depending on laser wavelength). The same objective collected SHG signals as epi-SHG images and via condenser lens (NA = 0.55) as forward-SHG images. All data were collected at a faster speed of 400 Hz using the Galvano scanning head of the Leica TCS SP8 CARS microscope. The high-resolution SEM images were obtained on a Zeiss Merlin microscope with an InLens detector. The nanostructures were imaged using low acceleration voltages (1–2 kV) and short working distances (3 mm). The AFM images were measured on a Dimension Icon AFM (AFM Icon-PT 2 from Bruker) using Al-coated Si probe tips (type Tap150Al-G from BudgetSensors) The measurements were carried out in non-contact mode in ambient air. Using a portable transfer method, the MoS<sub>2</sub> samples were transferred onto a TEM grid with a polymethylmethacrylate (PMMA) polymer. The TEPL measurements were performed using a nanoRaman system (XploRANano, HORIBA Scientific) integrating an atomic force microscope (SmartSPM) and a Raman microscope (XploRA) with a 100× WD objective tilted by 60° with respect to the sample plane for excitation and collection. A 532 nm excitation p-polarized laser was focused onto the cantilever-based silver-coated AFM-TERS tip (OMNI-TERS-SNC-Ag, Applied Nanostructures Inc.). The true nanoPL map was obtained from recording two PL maps in a special mode called “Spec-TopTM” mode with a “dual spec” option: for each pixel i) one spectrum (sum of the near-field and far-field signals) was acquired with the tip in direct contact with the surface with a typical interaction force of 2–10 nN and ii) another spectrum was acquired with the tip a few nm away from the sample surface, considered to be the far-field contribution. In between two pixels of the map, the sample moved in alternating contact to preserve the sharpness and plasmonic enhancement of the tip.

For STEM imaging, MoS<sub>2</sub> was transferred from the sapphire substrate to the TEM grid by PMMA coating, followed by the KOH etching technique. In this process, the PMMA A4 solution (concentration 10 mg/100 ml in anisole) produced a polymer film with a thickness of 100 nm. The MoS<sub>2</sub> sample on sapphire was spin-coated with PMMA at 3000 rpm speed, followed by heating on a hot plate at 120 °C for a few minutes. The PMMA layer acted as a handle layer to transfer the MoS<sub>2</sub> specimen from the sapphire substrate to the TEM grid. The sample region was then marked and scratched using a diamond cutter under the microscope. The marked area of the sample was usually smaller than the TEM grid. The specimen was then dipped into a 1% potassium hydroxide (KOH) solution for a few minutes. KOH intercalated between the sapphire and sample and easily detached the PMMA-coated MoS<sub>2</sub> from the sapphire substrate. Afterward, to remove KOH residue, the sample was transferred to a Petri dish containing deionized water, washed several times, and finally picked up by TEM grids. The specimens on the TEM grids were again cleaned in acetone vapor as PMMA could easily dissolve in acetone. After removing the PMMA, the samples were heated at 90 °C to ensure improved adhesion contact between MoS<sub>2</sub> and the TEM grid. The presence of the samples on the TEM grid after cleaning with acetone vapor was verified by Raman measurements. Finally, the MoS<sub>2</sub> samples were annealed at 250 °C in an Ar–H<sub>2</sub> flow (100 sccm flow rate) for two hours to remove the organic residue. The samples transferred on the TEM grid were baked at 160 °C in a vacuum for 8 h before loading to the STEM chamber for imaging. The STEM measurements were performed using an aberration-corrected Nion UltraSTEM 100 microscope equipped with a cold field emission gun. The images were acquired at an acceleration voltage of 60 kV and a semi-convergence angle of 31 mrad.

Using the above procedure, the as-grown MoS<sub>2</sub> nanoribbons were transferred to the Si substrate with a SiO<sub>2</sub> thickness of 300 nm at the top

surface. The drain-source contacts were patterned via UV photolithography of a Maskless Aligner using a 405 nm laser diode array. The electrical contacts Cr (10 nm)/Au (100 nm) were deposited by electron beam evaporation at a pressure of  $1 \times 10^{-6}$  mbar and a depositing rate of  $0.5 \text{ \AA s}^{-1}$ . The separation between the source-drain electrodes was 3  $\mu\text{m}$ . Then the devices were annealed at 300 °C in Ar-5% H<sub>2</sub> gas for 2 h. The optoelectrical studies were conducted in the ambient environment at room temperature using a dual-channel Keithley 2636A semiconductor analyzer, in which channel A was used to bias the source-drain electrodes, while channel B was to gate control the device. The photoresponse was measured using a probe tip connected to the Keithley 2636 Source, and the data acquisition was performed using KickStart software. The measurements were acquired under dark and illumination of various intensities of a 532 nm laser. In all measurements, the laser beam was defocused to a beam diameter of 4.12  $\mu\text{m}$  to ensure uniform illumination of the device.

**DFT Optimizations and STEM Simulations:** The MoS<sub>2</sub> nanoribbons were modeled by defect-free MoS<sub>2</sub> bi- and trilayers with different layer stackings. The different stackings were built based on single 1H-MoS<sub>2</sub> monolayers from the Computational 2D Materials Database.<sup>[60]</sup> Different stackings were created by rotating and/or shifting the layers to each other and optimizing the multilayer structure and the cell thereafter. The gap between the multilayers was chosen to be 20  $\text{\AA}$ . All considered stackings and their theoretical STEM results are given in Figure S7 (Supporting Information).

The optimizations were carried out using periodic density functional theory calculations within the projector augmented wave (PAW) method<sup>[61]</sup> using the atomic simulation environment<sup>[62]</sup> and the GPAW code.<sup>[63]</sup> The electron density was represented by plane waves with a cut-off of 900 eV. Exchange and correlation were treated by the Perdew–Burke–Ernzerhof functional<sup>[64]</sup> and reciprocal space was sampled with a k-point density of  $6 \text{ \AA}^{-1}$ . The theoretical STEM images and corresponding line profiles of the relaxed atomic structures were simulated using the abTEM code.<sup>[65]</sup> The parameters of the simulations were set to match the experimental setup, that is, an acceleration voltage of 60 kV and a semi-convergence angle of 31 mrad.

## Supporting Information

Supporting Information is available from the Wiley Online Library or from the author.

## Acknowledgements

S.C. acknowledges support from the Independent Research Fund Denmark, Sapere Aude grant (project number 8049-00095B). STEM imaging was conducted as a part of a user project at the Center for Nanophase Materials Sciences, ORNL, a DOE Office of Science User Facility.

## Conflict of Interest

The authors declare no conflict of interest.

## Data Availability Statement

The data that support the findings of this study are openly available in arXIV at <https://arxiv.org/submit/4790454>, reference number 4790454.

## Keywords

Molybdenum disulphide (MoS<sub>2</sub>), nanoribbons, pulsed laser deposition (PLD), photodetectors, second harmonic generation (SHG), tip-enhanced PL, Transition metal dichalcogenides (TMDs)

Received: March 16, 2023

Revised: May 4, 2023

Published online: June 25, 2023

- [1] X. Yang, Z. Shan, Z. Luo, X. Hu, H. Liu, Y. Zhang, X. Zhang, M. Shoaib, J. Qu, X. Yi, X. Wang, X. Zhu, Y. Liu, L. Liao, X. Wang, S. Chen, A. Pan, *ACS Nano* **2020**, *14*, 3397.
- [2] X. Yang, R. Wu, B. Zheng, Z. Luo, W. You, H. Liu, L. Li, Y. Zhang, Q. Tan, D. Liang, Y. Chen, J. Qu, X. Yi, X. Wang, J. Zhou, H. Duan, S. Wang, S. Chen, A. Pan, *ACS Nano* **2022**, *16*, 4371.
- [3] R. Bai, T. Xiong, J. Zhou, Y.-Y. Liu, W. Shen, C. Hu, F. Yan, K. Wang, D. Wei, J. Li, J. Yang, Z. Wei, *InfoMat* **2022**, *4*, e12258.
- [4] Z. Li, Z. Jiang, W. Zhou, M. Chen, M. Su, X. Luo, T. Yu, C. Yuan, *Inorg. Chem.* **2021**, *60*, 1991.
- [5] L. Zhang, Z. Wang, J. Zhang, B. Chen, Z. Liang, X. Quan, Y. Dai, J. Huang, Y. Wang, S.-J. Liang, M. Long, M. Si, F. Miao, Y. Peng, *Adv. Funct. Mater.* **2022**, *32*, 2204760.
- [6] M. Velický, A. Rodriguez, M. Bouša, A. V. Krayev, M. Vondráček, J. Honolka, M. Ah-madi, G. E. Donnelly, F. Huang, H. D. Abruña, K. S. Novoselov, O. Frank, *J. Phys. Chem. Lett.* **2020**, *11*, 6112.
- [7] Y. Zhao, K. Xu, F. Pan, C. Zhou, F. Zhou, Y. D. Chai, *Adv. Funct. Mater.* **2017**, *27*, 1603484.
- [8] D. Kufer, G. Konstantatos, *Nano Lett.* **2015**, *15*, 7307.
- [9] W. Yang, J. Shang, J. Wang, X. Shen, B. Cao, N. Peimyoo, C. Zou, Y. Chen, Y. Wang, C. Cong, W. Huang, T. Yu, *Nano Lett.* **2016**, *16*, 1560.
- [10] M.-L. Tsai, S.-H. Su, J.-K. Chang, D.-S. Tsai, C.-H. Chen, C.-I. Wu, L.-J. Li, L.-J. Chen, J.-H. He, *ACS Nano* **2014**, *8*, 8317.
- [11] Y. J. Zhang, T. Ideue, M. Onga, F. Qin, R. Suzuki, A. Zak, R. Tenne, J. H. Smet, Y. Iwasa, *Nature* **2019**, *570*, 349.
- [12] K. Chen, J. Deng, X. Ding, J. Sun, S. Yang, J. Z. Liu, *J. Am. Chem. Soc.* **2018**, *140*, 16206.
- [13] H. Xu, S. Liu, Z. Ding, S. J. R. Tan, K. M. Yam, Y. Bao, C. T. Nai, M.-F. Ng, J. Lu, C. Zhang, K. P. Loh, *Nat. Commun.* **2016**, *7*, 12904.
- [14] M. M. Pour, A. Lashkov, A. Radocea, X. Liu, T. Sun, A. Lipatov, R. A. Korlacki, M. Shekhirev, N. R. Aluru, J. W. Lyding, V. Sysoev, A. Sinitskii, *Nat. Commun.* **2017**, *8*, 820.
- [15] S. Li, S. Zhang, R. Zhao, *Nanoscale* **2022**, *14*, 8454.
- [16] S. P. Sasikala, Y. Singh, L. Bing, T. Yun, S. H. Koo, Y. Jung, S. O. Kim, *Nat. Commun.* **2020**, *11*, 5032.
- [17] D. Tang, M. Dan, Y. Zhang, *Nano Energy* **2022**, *104*, 107888.
- [18] Y. Li, E. C. Moy, A. A. Murthy, S. Hao, J. D. Cain, E. D. Hanson, J. G. DiStefano, W. H. Chae, Q. Li, C. Wolverton, X. Chen, V. P. Dravid, *Adv. Funct. Mater.* **2018**, *28*, 1704863.
- [19] R. Mupparapu, M. Steinert, A. George, Z. Tang, A. Turchanin, T. Pertsch, I. Staude, *Adv. Mater. Interfaces* **2020**, *7*, 2000858.
- [20] S. K. Alavi, B. V. Senkovskiy, D. Hertel, D. Haberer, Y. Ando, K. Meerholz, F. R. Fischer, A. Grueneis, K. Lindfors, *ACS Appl. Nano Mater.* **2020**, *3*, 8343.
- [21] X. Xiong, Q. Zhang, X. Zhou, B. Jin, H. Li, T. Zhai, *J. Mater. Chem. C* **2016**, *4*, 7817.
- [22] X. Li, B. Li, J. Lei, K. V. Bets, X. Sang, E. Okogbue, Y. Liu, R. R. Unocic, B. I. Yakobson, J. Hone, A. R. Harutyunyan, *Sci. Adv.* **2021**, *7*, eabk1892.
- [23] D. Wu, J. Shi, X. Zheng, J. Liu, W. Dou, Y. Gao, X. Yuan, F. Ouyang, H. Huang, *Phys. Status Solidi RRL* **2013**, *13*, 1900063.
- [24] H. Wang, L. A. Zepeda-Ruiz, G. H. Gilmer, M. Upmanyu, *Nat. Commun.* **2013**, *4*, 1956.
- [25] S. M. Poh, S. J. R. Tan, X. Zhao, Z. Chen, I. Abdelwahab, D. Fu, H. Xu, Y. Bao, W. Zhou, K. P. Loh, *Adv. Mater.* **2017**, *29*, 1605641.
- [26] F. Cheng, H. Xu, W. Xu, P. Zhou, J. Martin, K. P. Loh, *Nano Lett.* **2017**, *17*, 1116.

- [27] D. I. Miakota, G. Ghimire, R. Kumar Ulaganathan, M. E. Rodriguez, S. Canulescu, *Appl. Surf. Sci.* **2023**, 619, 156748.
- [28] D. I. Miakota, R. R. Unocic, F. Bertoldo, G. Ghimire, S. Engberg, D. Geohegan, K. S. Thygesen, S. Canulescu, *Nanoscale* **2022**, 14, 9485.
- [29] S. Canulescu, E. Papadopoulou, D. Anglos, T. Lippert, C. Schneider, A. Wokaun, *J. Appl. Phys.* **2009**, 105, 063107.
- [30] S. Li, Y.-C. Lin, W. Zhao, J. Wu, Z. Wang, Z. Hu, Y. Shen, D.-M. Tang, J. Wang, Q. Zhang, H. Zhu, L. Chu, W. Zhao, C. Liu, Z. Sun, T. Taniguchi, M. Osada, W. Chen, Q.-H. Xu, A. T. S. Wee, K. Suenaga, F. Ding, G. Eda, *Nat. Mater.* **2018**, 17, 535.
- [31] J. Lei, Y. Xie, A. Kutana, K. V. Bets, B. I. Yakobson, *J. Am. Chem. Soc.* **2022**, 144, 7497.
- [32] P. Yang, Z. Zhang, M. Sun, F. Lin, T. Cheng, J. Shi, C. Xie, Y. Shi, S. Jiang, Y. Huan, P. Liu, F. Ding, C. Xiong, D. Xie, Y. Zhang, *ACS Nano* **2019**, 13, 3649.
- [33] J. R. Esterlich, K. Affannoukoue, R. Kaupmees, D. Miakota, S. Engberg, M. Grossberg-Kuus, J. Schou, S. Canulescu, *Appl. Phys. A: Mater. Sci. Process.* **2023**, 129, 59.
- [34] F. Bertoldo, R. R. Unocic, Y.-C. Lin, X. Sang, A. A. Puretzky, Y. Yu, D. Miakota, C. M. Rouleau, J. Schou, K. S. Thygesen, D. B. Geohegan, S. Canulescu, *ACS Nano* **2021**, 15, 2858.
- [35] D. I. Miakota, G. Ghimire, R. Ulaganathan, M. Rodriguez, S. Canulescu, *Appl. Surf. Sci.* **2023**, 619, 156748.
- [36] J. Yan, J. Xia, X. Wang, L. Liu, J.-L. Kuo, B. K. Tay, S. Chen, W. Zhou, Z. Liu, Z. X. Shen, *Nano Lett.* **2015**, 15, 8155.
- [37] S. M. Shinde, K. P. Dhakal, X. Chen, W. S. Yun, J. Lee, H. Kim, J.-H. Ahn, *NPG Asia Mater.* **2018**, 10, e468.
- [38] X. Zhao, S. Ning, W. Fu, S. J. Pennycook, K. P. Loh, *Adv. Mater.* **2018**, 30, 1802397.
- [39] A. Yan, W. Chen, C. Ophus, J. Ciston, Y. Lin, K. Persson, A. Zettl, *Phys. Rev. B* **2016**, 93, 041420.
- [40] K. P. Dhakal, D. L. Duong, J. Lee, H. Nam, M. Kim, M. Kan, Y. H. Lee, J. Kim, *Nanoscale* **2014**, 6, 13028.
- [41] Z. Liu, et al., *Nat. Commun.* **2014**, 5, 5246.
- [42] M. Tosun, D. Fu, S. B. Desai, C. Ko, J. S. Kang, D.-H. Lien, M. Najmzadeh, S. Tongay, J. Wu, A. Javey, *Sci. Rep.* **2015**, 5, 10990.
- [43] X. Yin, Z. Ye, D. A. Chenet, Y. Ye, K. O'Brien, J. C. Hone, X. Zhang, *Science* **2014**, 344, 488.
- [44] K. Yao, S. Zhang, E. Yanev, K. McCreary, H.-J. Chuang, M. R. Rosenberger, T. Darlington, A. Krayev, B. T. Jonker, J. C. Hone, D. N. Basov, P. J. Schuck, *Adv. Opt. Mater.* **2022**, 10, 2200085.
- [45] Y. Li, Y. Rao, K. F. Mak, Y. You, S. Wang, C. R. Dean, T. F. Heinz, *Nano Lett.* **2013**, 13, 3329.
- [46] M. Zhao, Z. Ye, R. Suzuki, Y. Ye, H. Zhu, J. Xiao, Y. Wang, Y. Iwasa, X. Zhang, *Light: Sci. Appl.* **2016**, 5, e16131.
- [47] S. M. Shinde, K. P. Dhakal, X. Chen, W. S. Yun, J. Lee, H. Kim, J.-H. Ahn, *NPG Asia Mater.* **2018**, 10, e468.
- [48] K.-I. Lin, Y.-H. Ho, S.-B. Liu, J.-J. Ciou, B.-T. Huang, C. Chen, H.-C. Chang, C.-L. Tu, C.-H. Chen, *Nano Lett.* **2018**, 18, 793.
- [49] J. Qi, M. Yeganeh, I. Koltover, A. Yodh, W. Theis, *Phys. Rev. Lett.* **1993**, 71, 633.
- [50] L. Mennel, M. M. Furchi, S. Wachter, M. Paur, D. K. Polyushkin, T. Mueller, *Nat. Commun.* **2018**, 9, 516.
- [51] L. Mennel, M. Paur, T. Mueller, *APL Photonics* **2018**, 4, 034404.
- [52] S. Ghatak, A. N. Pal, A. Ghosh, *ACS Nano* **2011**, 5, 7707.
- [53] B. Radisavljevic, A. Radenovic, J. Brivio, V. Giacometti, A. Kis, *Nat. Nanotechnol.* **2011**, 6, 147.
- [54] Z. Deng, D. Cao, J. He, S. Lin, S. M. Lindsay, Y. Liu, *ACS Nano* **2012**, 6, 6197.
- [55] R. Frisenda, E. Giovanelli, P. Mishra, P. Gant, E. Flores, C. Sanchez, J. R. Ares, D. Perez de Lara, I. J. Ferrer, E. M. Perez, A. Castellanos-Gomez, *Chem. Commun.* **2017**, 53, 6164.
- [56] L. Wang, R. Chen, Z.-F. Ren, C.-W. Ge, Z.-X. Liu, S.-J. He, Y.-Q. Yu, C.-Y. Wu, L.-B. Luo, *Nanotechnology* **2016**, 27, 215202.
- [57] X. Xu, C. Fan, Z. Qi, S. Jiang, Q. Xiao, H. Liang, H. Duan, Q. Zhang, *ACS Appl. Nano Mater.* **2021**, 4, 9625.
- [58] B. Chitara, L. S. Panchakarla, S. B. Krupanidhi, C. N. R. Rao, *Adv. Mater.* **2011**, 23, 5419.
- [59] W. Song, Q. Liu, J. Chen, Z. Chen, X. He, Q. Zeng, S. Li, L. He, Z. Chen, X. Fang, *Small* **2021**, 17, 2100439.
- [60] M. N. Gjerding, A. Taghizadeh, A. Rasmussen, S. Ali, F. Bertoldo, T. Deilmann, N. R. Knosgaard, M. Kruse, A. H. Larsen, S. Manti, T. G. Pedersen, U. Petralanda, T. Skovhus, M. K. Svendsen, J. J. Mortensen, T. Olsen, K. S. Thygesen, *2D Mater.* **2021**, 8, 044002.
- [61] P. E. Blöchl, *Phys. Rev. B* **1994**, 50, 17953.
- [62] A. H. Larsen, J. J. Mortensen, J. Blomqvist, I. E. Castelli, R. Christensen, M. Dulak, J. Friis, M. N. Groves, B. Hammer, C. Hargus, E. D. Hermes, P. C. Jennings, P. B. Jensen, J. Kermode, J. R. Kitchin, E. L. Kolsbjerg, J. Kubal, K. Kaasbjerg, S. Lysgaard, J. B. Maronsson, T. Maxson, T. Olsen, L. Pastewka, A. Peterson, C. Rostgaard, J. Schiøtz, O. Schütt, M. Strange, K. S. Thygesen, T. Vegge, et al., *J. Phys.: Condens. Matter* **2017**, 29, 273002.
- [63] J. Enkovaara, C. Rostgaard, J. J. Mortensen, J. Chen, M. Dulak, L. Ferrighi, J. Gavnholt, C. Glinsvad, V. Haikola, H. A. Hansen, H. H. Kristoffersen, M. Kuisma, A. H. Larsen, L. Lehtovaara, M. Ljungberg, O. Lopez-Acevedo, P. G. Moses, J. Ojanen, T. Olsen, V. Petzold, N. A. Romero, J. Stausholm-Møller, M. Strange, G. A. Tritsarlis, M. Vanin, M. Walter, B. Hammer, H. Hakkinen, G. K. H. Madsen, R. M. Nieminen, et al., *J. Phys.: Condens. Matter* **2010**, 22, 253202.
- [64] J. P. Perdew, K. Burke, M. Ernzerhof, *Phys. Rev. Lett.* **1996**, 77, 3865.
- [65] J. Madsen, T. Susi, *Open Res. Europe* **2021**, 1, 13015.